

CHAPTER 4

ANALYSIS AND DESIGN OF THE DUAL INVERTED-F ANTENNA

4.1. Introduction

The previous chapter presented the Inverted-F Antenna (IFA) and its variations as antenna designs suitable for use in hand-held devices. This chapter presents modeling, construction, and measurements for the IFA and the Dual Inverted-F Antenna (DIFA). Also, the effects of a size-limited ground plane are investigated by modeling and building the antennas on conducting boxes of various dimensions. The antennas are classified according to currents on the antenna structure, input impedance, far-field radiation pattern, and polarization. In Section 4.2 an algorithm is developed that applies the Method of Moments (MoM) to solve the Electric Field Integral Equation (EFIE) for wire radiators in free space. In Section 4.3, the MoM algorithm developed in Section 4.2 is applied to wire representations of the IFA and DIFA. The MoM algorithm is applied to the conducting boxes using a wire grid representation. Section 4.4 discusses the construction of the IFA and DIFA and the measurement of impedance, radiation pattern, and gain along with comparison to the model calculations. Section 4.5 contains concluding remarks.

4.2. Numerical Techniques

4.2.1. The Method of Moments Applied to Wire Antennas

In Chapter 3, the input impedance and far-field radiation patterns of the Inverted-L Antenna (ILA) were derived by assuming a current distribution over the antenna. In practice, the current distribution on an antenna is rarely known. One method used to model the currents on an arbitrarily shaped antenna is the Method of Moments (MoM). For wire antennas, the MoM is used to implement a piecewise solution of the electric field integral equation (EFIE) for cylindrical conductors of vanishing volume. [1] The magnetic field integral equation (MFIE) fails for infinitesimal volume, and is used to solve the fields due to surface currents on large, smooth, closed, and volumous perfectly conducting objects. [1] This discussion involves the application of the EFIE to wire antennas.

The MoM is used to solve equations of the form

$$Lf = e \quad (4.1)$$

where e is a known excitation, L is a linear operator, and f is an unknown response. [1] Thus, the MoM is readily applied to integral equations of the form [2]

$$\int I(z')K(z, z')dz' = -E^i(z) \quad (4.2)$$

This is the form of Pocklington's Integral Equation derived in Section 3.3. The general form of Pocklington's Integral Equation using the thin wire approximation is

$$-E^i(z) = \frac{1}{j\omega\epsilon_o} \int_{-L/2}^{L/2} \left(\frac{\partial^2 \Psi(z, z')}{\partial z'^2} + \beta^2 \Psi(z, z') \right) I(z') dz' \quad (4.3)$$

where z is the observation point, z' is the source location, Ψ is the free space Green's function, and k is the wave number. In (4.3), the known excitation is the incident or impressed field, $E^i(z)$. The linear operator is the integral operator

$$K(z, z') = \frac{\partial^2 \Psi(z, z')}{\partial z'^2} + \beta^2 \Psi(z, z') \quad (4.4)$$

and the unknown response is the current on the antenna, $I(z')$. The general form of Pocklington's Equation is one dimensional. A generalized three-dimensional geometry is illustrated in Figure 4.1.

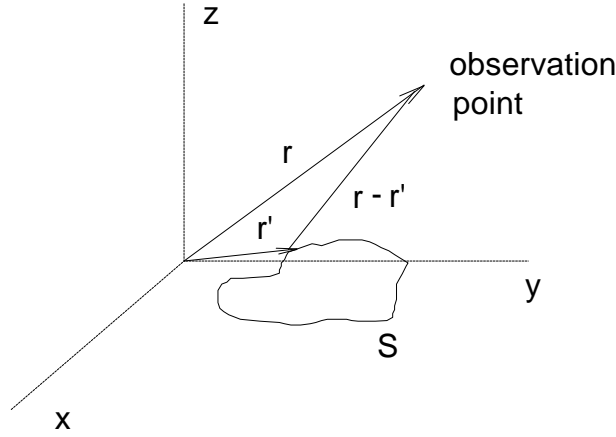


Figure 4.1. A generalized three-dimensional geometry

For the geometry in Figure 4.1, the EFIE is

$$\mathbf{E}(\mathbf{r}) = \frac{-j\eta}{4\pi k} \int_V \mathbf{J}(\mathbf{r}') \cdot \mathbf{G}(\mathbf{r}, \mathbf{r}') dV' \quad (4.5)$$

where

$$\mathbf{G}(\mathbf{r}, \mathbf{r}') = \left(k^2 g(\mathbf{r}, \mathbf{r}') + \nabla \nabla g(\mathbf{r}, \mathbf{r}') \right)$$

$$g(r, r') = \frac{e^{-jk|\mathbf{r}-\mathbf{r}'|}}{|\mathbf{r}-\mathbf{r}'|}$$

and η is the complex impedance of free space. The time convention is $e^{j\omega t}$. [1] For a perfectly conducting body, (4.5) reduces to

$$\mathbf{E}(\mathbf{r}) = \frac{-j\eta}{4\pi k} \int_S \mathbf{J}_s(\mathbf{r}') \cdot \mathbf{G}(\mathbf{r}, \mathbf{r}') dA' \quad (4.6)$$

where \mathbf{J}_s is the surface current density and the observation point, \mathbf{r} , must be off the surface of the conductor to prevent a singularity. [1] The boundary condition when the observation point approaches the surface of the conductor as a limit is

$$\mathbf{n}(\mathbf{r}) \times [\mathbf{E}^s(\mathbf{r}) + \mathbf{E}^i(\mathbf{r})] = 0 \quad (4.7)$$

where $\mathbf{n}(\mathbf{r})$ is the unit normal vector to the surface at \mathbf{r} and \mathbf{E}^s is the scattered field due to the surface current \mathbf{J}_s . [1] Using this boundary condition and (4.6), an integral equation is derived that gives the vector current density, \mathbf{J}_s , induced on an arbitrary surface S by an incident or impressed field \mathbf{E}^i . The generalized EFIE,

$$-\mathbf{n}(\mathbf{r}) \times \mathbf{E}^i(\mathbf{r}) = \frac{-j\eta}{4\pi k} \mathbf{n}(\mathbf{r}) \times \int_S \mathbf{J}_s(\mathbf{r}') \cdot (k^2 g(\mathbf{r}, \mathbf{r}') + \nabla \nabla g(\mathbf{r}, \mathbf{r}')) dA' \quad (4.8)$$

applies to a surface of arbitrary shape. [1] Assuming that the surface is a thin, cylindrical wire, (4.8) is reduced to a scalar equation by neglecting circumferential currents and variations in longitudinal current around the circumference of the wire. [1] The current is transformed into an equivalent filamentary line source at the axis of the wire. This allows the boundary condition to be applied at the surface of the cylindrical wire while avoiding singularities in the EFIE. Alternately, as discussed in Section 3.3, the current can be assumed to exist at the surface of the wire with the boundary condition enforced at the axis of the wire if the wire is cylindrical. [1] This method models charge discontinuities at steps in wire radius more accurately. When a filamentary current is used, the solution tends to converge with continuous charge distribution across the step in radius. However, it is known that more charge should exist on the wire with larger radius. [1]

Representing the current on the surface of the cylindrical wire as a filament separated by the wire radius, a , from the axis of the wire (see Figure 3.5(b)), (4.8) reduces to an integration along the length of the effective line source. Thus, (4.8) is rewritten as

$$-\mathbf{s} \cdot \mathbf{E}^i(\mathbf{r}) = \frac{-j\eta}{4\pi k} \int_L I(s') \left(k^2 \mathbf{s} \cdot \mathbf{s}' + \frac{\partial^2}{\partial s \partial s'} \right) g(\mathbf{r}, \mathbf{r}') ds' \quad (4.9)$$

which is a scalar equation where \mathbf{s} is a unit vector tangent to the surface of the wire, and \mathbf{s}' is a unit vector tangent to the axis of the wire.

The EFIE in (4.9) is of the form in (4.2). Therefore, the MoM is used to determine the unknown distribution $I(s')$. The process is widely known and is summarized here. Complete discussions are found in [3], and [2].

To implement the MoM, the antenna is modeled by N current segments. The current on the antenna is the sum of j basis functions, f_j on the j^{th} segment. Thus,

$$I(s') = \sum_{j=1}^N \alpha_j f_j \quad (4.10)$$

To solve for the unknown coefficients, α_j , a set of linear equations is established by taking the inner product of (4.1) with a set of weighting functions, $\{w_i\}$. [1] The number of weighting functions is chosen to equal the number of basis functions. Thus, the number of equations is equal to the number of unknown coefficients in (4.10), and (4.1) is rewritten as

$$\sum_{j=1}^N \alpha_j \langle w_i, Lf_j \rangle = \langle w_i, e \rangle \quad (4.11)$$

where

$$\langle f, g \rangle = \int_S f(\mathbf{r}) g(\mathbf{r}) dA$$

In matrix form, (4.11) becomes

$$[G][A] = [E] \quad (4.12)$$

where $G_{ij} = \langle w_i, Lf_j \rangle$, $A_j = \alpha_j$, and $E_i = \langle w_i, e \rangle$. The relation in (4.12) is solved using a matrix inversion routine to yield the unknown coefficients in (4.11).

4.2.2. The Numerical Electromagnetics Code (NEC)

Several efficient codes are commercially available that perform the MoM. One such code is the Numerical Electromagnetics Code (NEC) which was developed by the government. The latest version of NEC is NEC4 which allows improved accuracy and fast convergence for electrically small antennas. [1]

4.2.2.1. Current Basis and Weighting Functions

NEC4 implements the MoM algorithm developed in (4.10) through (4.12) using the EFIE in (4.9). The weighting functions are a series of delta functions at the segment centers. [1] This is a process called point matching that is point sampling of the integral equation at the center of each segment. [1]

The basis function used by NEC4 is a three term sinusoidal current expansion given by

$$I_j(s) = A_j + B_j \sin k_s(s - s_j) + C_j [\cos k_s(s - s_j) - 1] \quad |s - s_j| < \frac{\Delta_j}{2} \quad (4.13)$$

where s_j is the value of s at the center of segment j , and Δ_j is the segment length. Such an expansion was shown to provide rapid solution convergence, especially for long wires. [1] The basis function used by NEC4 shows better results for electrically small wires than previous versions of NEC. [1] Two of the coefficients in (4.13) are eliminated by imposing continuity conditions at the segment ends. [1] At a junction between two wires, the continuity condition is that the change in the current and charge be constant, or

$$\frac{dI(s)}{ds} = -j\omega q(s) \quad (4.14)$$

where $I(s)$ is the current, and $q(s)$ is the charge at the junction. At a three or more wire junction, the currents are solved using Kirchhoff's Law that requires the currents into a node to sum to zero. The charge distribution at a three or more wire junction is less obvious, and a solution is available in the literature. [1] The current at a free wire end must go to zero. The current segment at the free end of a wire is called an end cap. The

NEC basis function is derived such that the current on a segment with no immediate neighbor goes to zero at the center, not the end of the segment (i.e. $A_j = 0$). [1] Therefore, a proportionality constant must be included in the basis function such that the current at the free end of an end cap goes to zero. If there is not an end cap, the proportionality constant is set to zero. [1] A rigorous derivation of the basis function used by NEC4 is found in the literature. [1]

4.2.2.2. Feed Technique

It is very important to accurately model voltage sources in the MoM analysis since errors are reflected in the input impedance calculation and therefore in the gain and other related quantities. [1] The NEC4 models developed in this chapter use the applied field or gap source model. For a source voltage V_i on segment i with length Δ_i , the field at the segment center (the match point) is defined as [1]

$$E_i = \frac{V_i}{\Delta_i} \quad (4.16)$$

The field at all match points without sources is set to zero. [1] The best results are obtained when the length of the segments on either side of the source segment are equal to Δ_i . The use of unequal segment lengths in the source region results in inaccurate input impedance results. [1] The input impedance is calculated using the voltage, V_i , at the center of the source segment, and the current at the center of the segment, I_i , as [1]

$$Z_{in} = \frac{V_i}{I_i} \quad (4.17)$$

This assumes that the source segment is short enough that the current over its length is relatively constant. [1]

4.2.2.3. Derivation of Antenna Fields

The electric fields from each wire segment are a combination of the fields due to each component function in (4.13). The fields due to the constant, $\sin k_s s$, and $\cos k_s s$ terms in the basis function are evaluated using the derived constants, B_j and C_j in (4.13). [1] The current is assumed to exist on the cylindrical surface of a wire with its axis along the z -axis of a cylindrical coordinate system. The currents are first integrated over z , and then over ϕ . Terms due to point charges at the end of segments are dropped since current continuity is enforced using Kirchhoff's Law in the basis function. [1] For a filamental current extending from z_1 to z_2 along the z -axis, the fields resulting from the current distribution

$$I(z') = I_0 \begin{pmatrix} \sin kz' \\ \cos kz' \end{pmatrix} \quad (4.18)$$

are [1]

$$E_\rho(\rho, z) = \frac{-j\eta I_0}{4\pi\rho} \frac{e^{-jkR}}{R} \left[(z - z') \begin{pmatrix} \cos kz' \\ -\sin kz' \end{pmatrix} - j \begin{pmatrix} \sin kz' \\ \cos kz' \end{pmatrix} \right] \Bigg|_{z'=z_1}^{z'=z_2} \quad (4.19)$$

$$E_z(\rho, z) = \frac{-j\eta I_0}{4\pi} \frac{e^{-jkR}}{R} \left[\begin{pmatrix} \cos kz' \\ -\sin kz' \end{pmatrix} \right] \Bigg|_{z'=z_1}^{z'=z_2} \quad (4.20)$$

and from the constant current I_0 are [1]

$$E_\rho(\rho, z) = 0 \quad (4.21)$$

$$E_z(\rho, z) = \frac{-j\eta I_0 k}{4\pi} \int_{z_1}^{z_2} \frac{e^{-jkR}}{R} dz' \quad (4.22)$$

where

$$R = [\rho^2 + (z - z')^2]^{1/2} \quad (4.23)$$

Using (4.19) through (4.22), the fields due to a tubular current distribution are derived by integrating over ϕ . Thus, the fields from each segment of wire are evaluated as [1]

$$E_{\rho}(\rho, z) = \frac{-j\eta I_0}{4\pi} \left[G_2(z - z') \begin{pmatrix} \cos kz' \\ -\sin kz' \end{pmatrix} - jG_3 \begin{pmatrix} \sin kz' \\ \cos kz' \end{pmatrix} \right]_{z'=z_1}^{z'=z_2} \quad (4.24)$$

$$E_z(\rho, z) = \frac{j\eta I_0}{4\pi} G_1 \left[\begin{pmatrix} \cos kz' \\ -\sin kz' \end{pmatrix} \right]_{z'=z_1}^{z'=z_2} \quad (4.25)$$

$$E_z(\rho, z) = \frac{-j\eta I_0 k}{4\pi} G_4 \quad (4.26)$$

where

$$G_1 = \frac{1}{2\pi} \int_0^{2\pi} \frac{e^{-jkR}}{R} d\phi \quad (4.27)$$

$$G_2 = \frac{1}{2\pi} \int_0^{2\pi} \frac{\cos \alpha}{p'} \frac{e^{-jkR}}{R} d\phi \quad (4.28)$$

$$G_3 = \frac{1}{2\pi} \int_0^{2\pi} \frac{\sin \alpha}{p'} e^{-jkR} d\phi \quad (4.29)$$

$$G_4 = \frac{1}{2\pi} \int_0^{2\pi} \int_{z_1}^{z_2} \frac{e^{-jkR}}{R} dz' d\phi \quad (4.30)$$

and

$$\cos \alpha = \frac{\rho - a \cos \phi}{p'} \quad (4.31)$$

$$p' = (\rho^2 + a^2 - 2\rho a \cos \phi)^{1/2} \quad (4.32)$$

with

$$R = (\rho^2 + a^2 + z^2 - 2\rho a \cos \phi)^{1/2} \quad (4.33)$$

where a is the radius of the current tube, or cylindrical wire segment. The factors G_1 through G_4 are estimated as [1]

$$G_1 \approx \frac{e^{-jkR_t}}{R_t} \quad (4.34)$$

$$G_2 \approx \frac{e^{-jkR_t}}{\rho R_t} \quad (4.35)$$

$$G_3 \approx \frac{e^{-jkR_t}}{\rho} \quad (4.36)$$

$$G_4 \approx \int_{z_1}^{z_2} \frac{e^{-jkR_t}}{R_t} dz' \quad (4.37)$$

where

$$R_t = [\rho^2 + a^2 + (z - z')^2]^{1/2} \quad (4.38)$$

The derivation of the approximation is available in the literature. [1] The expressions in (4.24) through (4.26) are evaluated using the currents determined by the MoM analysis to calculate the electric fields produced by each wire segment. A similar derivation is carried out to produce an expression for the magnetic fields from each wire segment. Special expressions are required at wire ends and for surface currents. [1] The electric and magnetic fields from each current segment are combined to produce the fields of the antenna.

4.2.2.4. Modeling Guidelines

The MoM algorithm used by NEC4 is subject to the thin wire and current segmentation approximations. To ensure proper convergence of the numerical model, a number of guidelines must be followed during development. The remainder of this section defines guidelines to follow while developing models in NEC4.

First, the accuracy of the numerical current model depends on the resolution of the MoM current segmentation. This limits the length of the segments, Δ . [4] In general, Δ should be less than 0.1λ . Longer segments are acceptable on long straight wires. Much shorter segments should be used at bends. NEC4 allows the use of very short segments. However, a lower bound is placed on segment length by the thin wire approximation. Errors occur due to instabilities in the current at wire ends if Δ/a is less than 0.5 where a is the wire radius. Segments lengths much larger than this should be used if possible. [4]

The thin wire approximation also limits the radius of the wire. If the wire is thick enough to allow circumferential currents or variation of the longitudinal current around the circumference of the wire, the numerical solution is inaccurate. The NEC4 solution is only valid if $2\pi a / \lambda$ is much less than one. [4] The guidelines for modeling wire antennas using NEC are summarized in Table 4.1.

Table 4.1. Summary of NEC Modeling Guidelines

#	Guideline
1	The length of the segment, Δ , must be less than 0.1λ except on long straight wires
2	Δ/a must be greater than 0.5 where a is the wire radius and Δ is the segment length
3	$2\pi a / \lambda$ must be much less than one where a is the wire radius

This section has described the MoM algorithm used by NEC4 to model the currents on antennas of arbitrary shape. In addition, modeling guidelines for wire antennas were presented. These guidelines along with graphical convergence checks are used to improve the accuracy and reliability of numerical results generated by NEC4. In the next section, the validity of the MoM algorithm used by NEC4 is checked and a convergence test is implemented to demonstrate the proper MoM segmentation for the Dual Inverted-F Antenna.

4.2.3. Validation of Modeling Techniques

The Method of Moments (MoM) algorithm described in the previous section used the electric field integral equation (EFIE) to model the currents on arbitrarily shaped wire antennas. In this section, the validity of the algorithm is tested.

4.2.3.1 Comparison to Published Data

In this subsection, the Radiation Coupled Dual-L Antenna (RCDLA) in Figure 4.2 is used to test the validity of the MoM algorithm developed in Section 4.2.1. The RCDLA described in [5] is similar to the DIFA except that the horizontal segments are narrow plates.

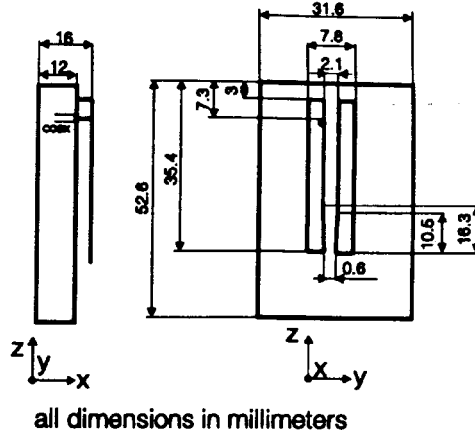


Figure 4.2. The Radiation Coupled Dual-L Antenna and resonant dimensions for $f = 1895$ MHz.

Validation of the MoM algorithm in Section 4.2.1 is achieved by modeling the RCDLA using NEC4 and comparing the computed results to those published in [5]. The EFIE used by NEC4 was developed to model cylindrical wires of vanishing volume. Therefore, the planar elements in the RCDLA are replaced with a wire mesh of equal dimensions. The currents on the wire mesh are assumed to approximate the surface currents on the planar elements. The wire mesh representation gives good results for far-field pattern and polarization, but has been shown to cause error in near field quantities such as input impedance. [1] The simulated and measured radiation patterns of the RCDLA at a frequency of 1895 MHz are illustrated in Figure 4.3. [5] Figure 4.3 shows simulated patterns, generated using an MoM algorithm, and measured patterns.

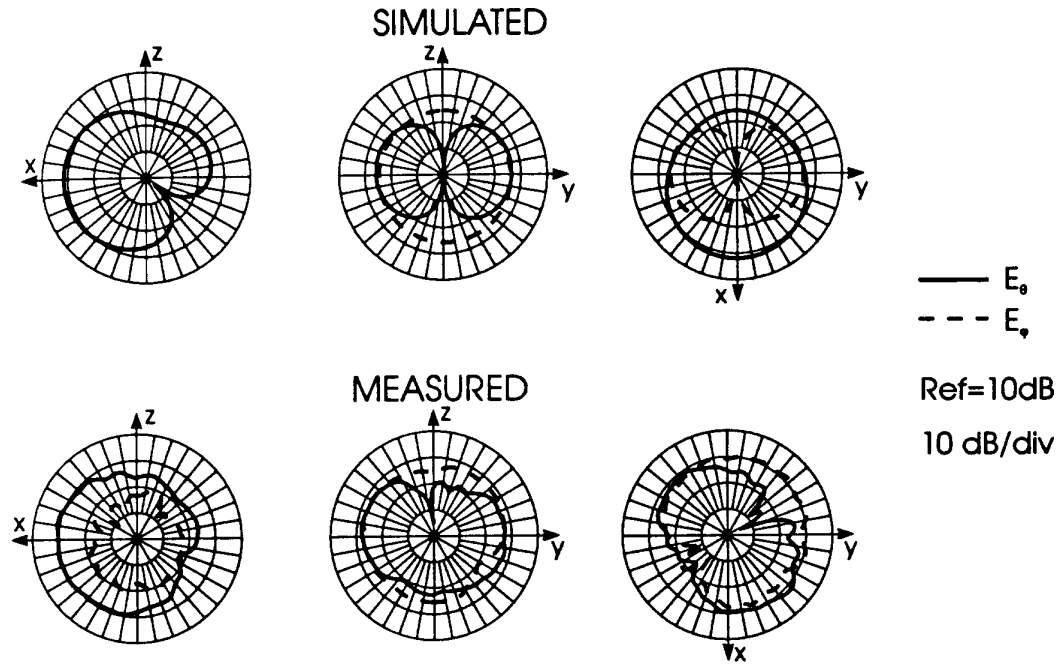


Figure 4.3. Measured and simulated radiation patterns for the RCDLA in Figure 4.2. The simulated patterns were generated using the Method of Moments with a wire grid representation of the planar surfaces at $f = 1895$ MHz. [5]

In order to test the NEC4 algorithm, a model of the RCDLA in Figure 4.2 was developed and implemented using NEC4. A square wire mesh constructed using wire segments of length, $l = 0.02\lambda$ was used to model the planar surfaces. The choice of mesh dimension was arbitrary since the mesh size used in [5] was not specified. The resulting patterns, calculated using NEC4, are illustrated in Figure 4.4.

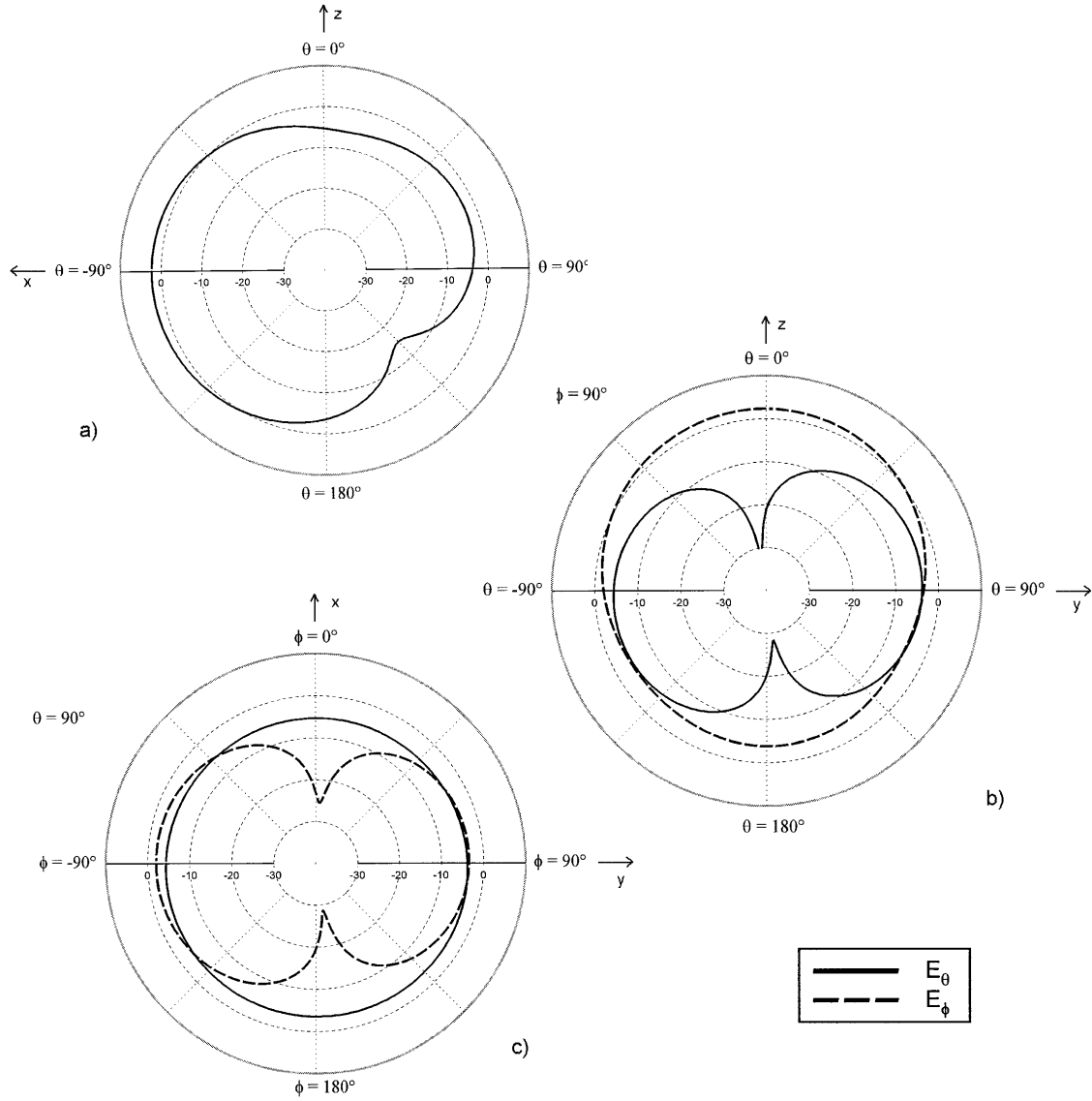


Figure 4.4. Radiation Patterns of the RCDLA modeled using NEC4 and wire gridding.

a) Pattern in the x-z plane. b) Pattern in the y-z plane. c) Pattern in the x-y plane.

All patterns are 10 dB/div with a 10 dB reference level.

Comparison of Figures 4.4 and 4.3 shows that the RCDLA radiation patterns produced by NEC4 closely match the simulated patterns in [5]. The patterns are in terms of gain. The simulated gains in [5] were higher than modeled by NEC4. In both cases, a null was formed in the x-z plane under the conducting box. The null was deeper in the published data, but was formed at the same angle as predicted by NEC4. Overall, the pattern shapes

predicted by NEC4 in all three principal planes matched the published patterns for the RCDLA to an acceptable degree of accuracy.

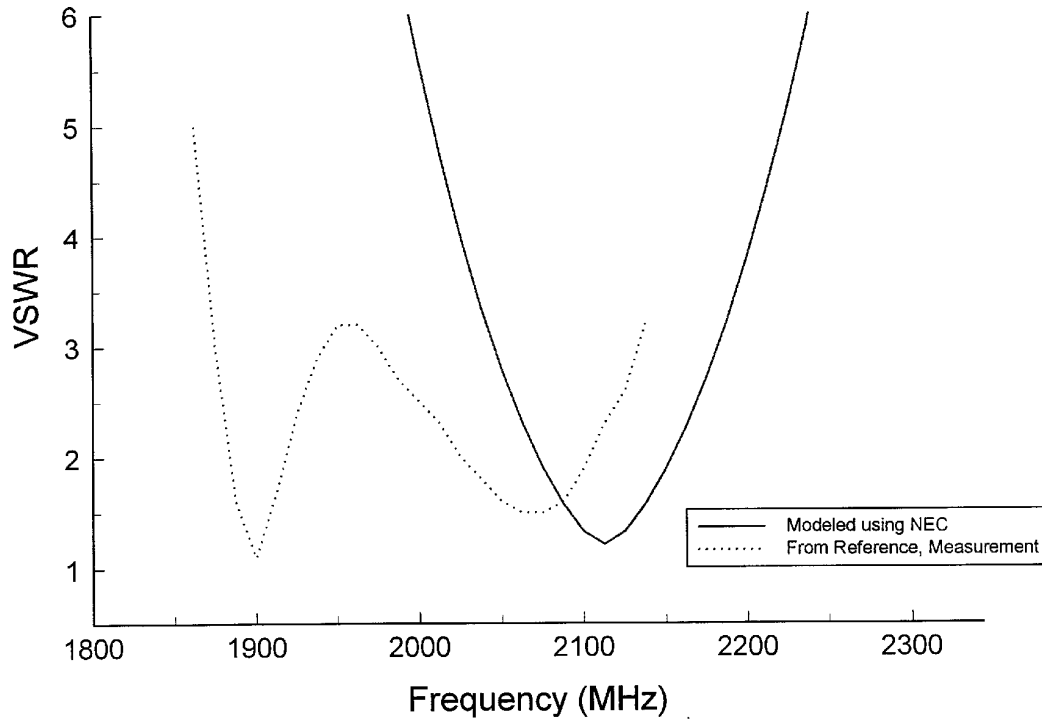


Figure 4.5. The measured input impedance of the RCDLA compared with the prediction of input impedance by NEC4. [5]

The input impedance for the RCDLA is shown in Figure 4.5 as calculated by NEC4, and compared to measured data from [5]. As illustrated in Figure 4.5, NEC4 did not accurately predict the input impedance of the RCDLA. The measured RCDLA input impedance contains two distinct resonant frequencies. NEC predicted a single resonant frequency. The resonance predicted by NEC was at a higher frequency than either of the measured resonances. The discrepancy between modeled and measured input impedance data suggests that either the NEC4 algorithm is not modeling the currents correctly, or there are slight differences between the numerical RCDLA models. Specifically, the wire mesh used in the two models is different because the dimensions of the mesh used in [5]

were not specified. In any case, special care is necessary to verify the accuracy of antenna input impedances modeled using NEC.

In summary, the radiation patterns calculated by NEC4 for the RCDLA in Figure 4.4 matched the simulated results in Figure 4.3 published in [5] to an acceptable degree of accuracy. However, Figure 4.5 showed that the RCDLA input impedance calculated using NEC4 did not accurately match the results in [5]. Therefore, empirical measurement is necessary to validate discussions involving NEC4 input impedance calculations. This section has shown that the MoM algorithm developed in Section 4.2.1 accurately models antennas of arbitrary geometry that include planar surfaces. In the next section, a general MoM model of the Dual Inverted-F Antenna (DIFA) is established.

4.2.3.2 Application to the Dual Inverted-F Antenna

The Method of Moments (MoM) requires expansion of the current on an antenna into N current subsections. The solution of the antenna current distribution is a sum of the current expansions on the subsections. If the current is not expanded properly, or assumptions regarding the form of the current are ignored, the sum of the current expansions will not equal the current distribution on the antenna and the numeric result will not converge to an accurate solution. Section 4.2.2.4 presented a number of guidelines to follow when modeling wire antennas in NEC4. In this section, these guidelines are used along with convergence tests to develop a numerical model of the Dual Inverted-F Antenna (DIFA) that converges to a correct result. In other words, this section develops a model of the DIFA such that the summation of the current expansions on the subsections equals the actual current distribution on the DIFA within an acceptable margin of error. This subsection does not address the design issues of the DIFA. Once the model in this subsection is established, it is used in the next section to study the design issues of the Inverted-F Antenna (IFA) and the DIFA.

The DIFA is identical to the Radiation Coupled Dual-L Antenna presented in Section 4.2.3.1 with the exception that the horizontal planar elements are replaced by cylindrical wires of radius a . The DIFA in Figure 4.6 is operated against a ground plane

that can be modeled as infinite or size constrained. In this section the ground plane is considered infinite. The behavior of the DIFA over a size-limited ground plane is the subject of Section 4.3.3.2.

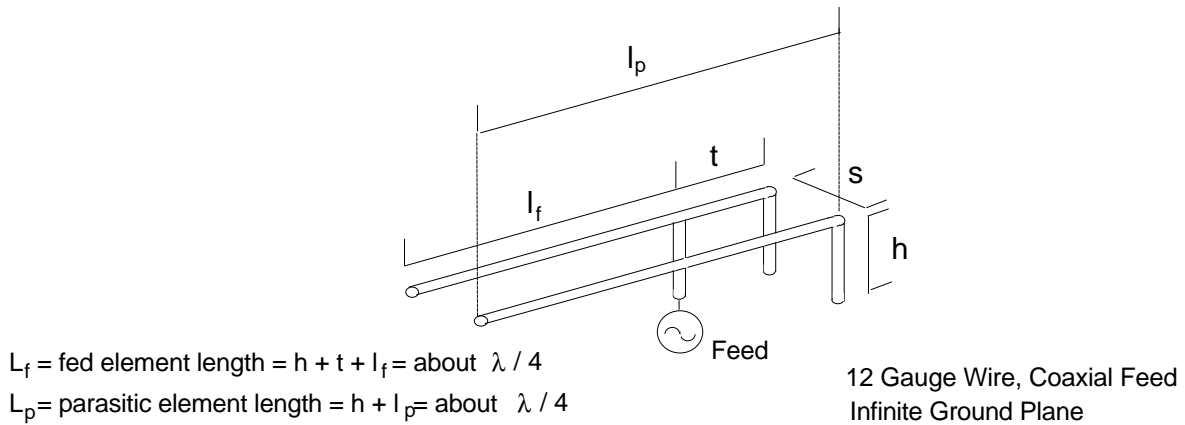


Figure 4.6. The DIFA operated against an infinite ground plane with dimensions noted.

For reference, the geometry of the DIFA in Figure 4.6 is broken into six thin cylindrical wires as noted in Figure 4.7.

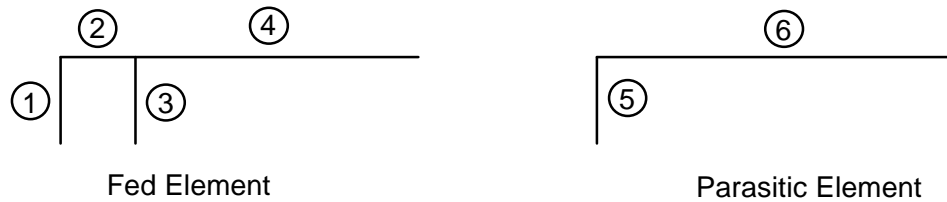


Figure 4.7. Wire divisions on the dual inverted-F antenna

The DIFA in Figure 4.6 was designed for use with the IVDS system described in Section 1.3. The DIFA was designed to resonate at 915 MHz and cover the ISM band between 902 and 928 MHz. The resonant dimensions of the DIFA are listed in Table 4.2.

Table 4.2. The resonant dimensions of the DIFA in Figure 4.6.

Wire Number	Symbol	Quantity
1	h	0.046λ
2	t	0.016λ
3 (feed probe)	h	0.046λ
4	l_f	0.204λ
5	h	0.046λ
6	l_p	0.195λ
Wire Radius	a	0.0024λ
Feed Probe Radius	a_f	0.0015λ
Element Spacing	s	0.022λ

To implement the MoM algorithm, the wires in Table 4.2 are subdivided into N_w segments where the subscript refers to the wire number. The current basis and weighting functions are applied over the subsections. Small values of N_w result in long segments that limit the resolution and accuracy of the numerical results. Large values of N_w increase the complexity of the model and require extensive computation time. The solution is to adjust $N = \sum_w N_w$ so that accurate results are achieved with minimal computation time. As N increases, the amount of error in the numerical result decreases. To test for numerical convergence, the DIFA specified in Table 4.2 is modeled using a gradually increasing number of segments. Comparison of the results indicates the point of convergence. A convergence test is performed by calculating the input impedance of the DIFA using NEC4 and the segmentations listed in Table 4.3. The calculated input impedance for the DIFA segmentations in Table 4.3 are compared in Figure 4.8.

Table 4.3. Segmentation data for MoM DIFA convergence test

Number	N_1	N_2	N_3	N_4	N_5	N_6	N
1	3	4	4	8	3	8	30
2	3	4	4	13	3	13	40
3	3	5	4	17	3	17	49
4	4	5	4	21	4	21	59
5	4	6	4	25	4	25	68
6	4	6	4	30	4	30	78
7	4	6	4	35	4	35	88

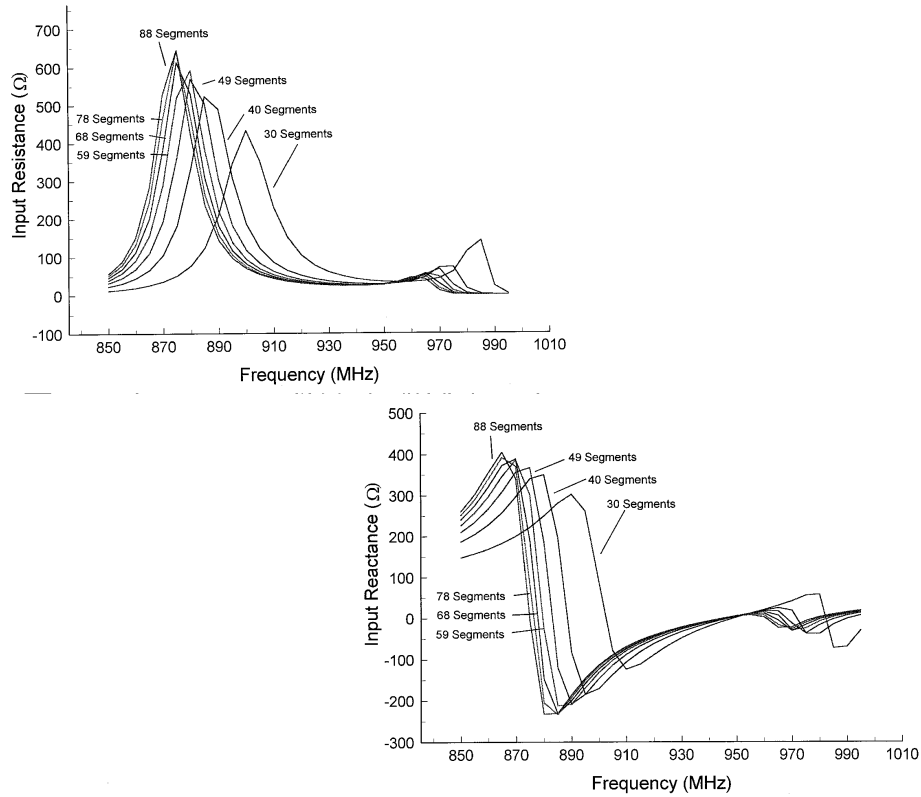


Figure 4.8. Impedance data from convergence test of DIFA in Table 4.3

Since input reactance is a near-field quantity, it converges slower than far-field radiation pattern and polarization. Therefore, convergence of the input impedance also indicates convergence of radiation pattern and polarization. Figure 4.8 shows that the impedance data converges when $N = 78$ segments are used to model the DIFA. If more than 78 segments are used, the improvement in accuracy is not worth the additional computation time required. Therefore, design 6 in Table 4.3 is applied to the models in the remainder of the chapter.

Guidelines for modeling wire antennas using NEC4 were presented in Table 4.1. The solution calculated by NEC4 using $N = 78$ segments is only valid if N_w on each wire satisfies all three of the guidelines in Table 4.1. Table 4.4 shows that the modeling guidelines in Table 4.1 are satisfied when the DIFA is divided into 78 segments according to design 6 in Table 4.3. This, along with the data shown in Figure 4.8, provides necessary and sufficient proof that the numerical model of the DIFA converges to the correct answer. In the next section, the MoM model developed in this section is applied to study the design issues the Inverted-F Antenna (IFA) the DIFA over infinite and size-limited ground planes.

Table 4.4. Validation of modeling guidelines for the DIFA in Figure 4.6.

Condition #1: $\Delta = \text{Segment Length} < 0.1\lambda$			
Condition #2: $\Delta/a > 0.5$ $a = \text{Radius of Wire}$			
Condition #3: $2\pi a / \lambda \ll 1$			
Wire Number	Quantity	Value	Meets Condition?
1	Δ	0.0115λ	1: Yes
	Δ/a	14.38	2: Yes
	$2\pi a / \lambda$	0.015	3: Yes
2	Δ	0.0027λ	1: Yes
	Δ/a	3.38	2: Yes
	$2\pi a / \lambda$	0.015	3: Yes
3	Δ	0.0115λ	1: Yes
	Δ/a	23.00	2: Yes
	$2\pi a / \lambda$	0.009	3: Yes
4	Δ	0.0068λ	1: Yes
	Δ/a	8.50	2: Yes
	$2\pi a / \lambda$	0.015	3: Yes
5	Δ	0.0115λ	1: Yes
	Δ/a	14.38	2: Yes
	$2\pi a / \lambda$	0.015	3: Yes
6	Δ	0.0065λ	1: Yes
	Δ/a	8.13	2: Yes
	$2\pi a / \lambda$	0.015	3: Yes